Experimental validation of magnetic control strategy in LCCS compensated wireless power transfer systems

Received: 2 November 2023 | Revised: 11 March 2024 | Accepted: 3 May 2024

IET Power Electronics

DOI: 10.1049/pel2.12718

The Institution of Engineering and Technology WILEY

ORIGINAL RESEARCH

Experimental validation of magnetic control strategy in LCC-S compensated wireless power transfer systems

Luigi Solimene[1] | **Fabio Corti**[2] | **Salvatore Musumeci**[1] | **Francisco Javier López-Alcolea**[3] | **Alberto Reatti**[2] | **Carlo Stefano Ragusa**[1]

[1]Department of Energy "Galileo Ferraris", Politecnico di Torino, Torino, Italy

[2]Department of Information Engineering, Università di Firenze, Firenze, Italy

[3]Escuela Técnica Superior de Ingeniería Industrial, Universidad de Castilla-La Mancha, Ciudad Real, Spain

Correspondence
Luigi Solimene, Energy Department "Galileo Ferraris", Politecnico di Torino, Torino 10129, Italy.
Email: luigi.solimene@polito.it

Abstract

The paper explores the use of the magnetic control strategy for the output power regulation of an LCC-S compensated inductive wireless power transfer system. The magnetic control is implemented through a controlled variable inductor whose magnetization state is actively regulated by an auxiliary DC–DC converter. The principles for the design and regulation of the system are discussed, and the experimental setup for the validation of the regulation method is implemented. Several measurement results highlight the effectiveness and potential improvements of the magnetic control strategy for inductive wireless power transfer systems.

1 | INTRODUCTION

The concept of wireless energy transmission has historical roots, but the advancement of high-power wireless systems is a relatively recent development. The evolution of high-frequency power electronic converters has made this progress possible. Wireless power transfer (WPT) technology has seen significant growth in power applications in recent years [1]. A WPT system allows power transfer from a source to a load, avoiding the connection through bulky cables and connectors, which are parts exposed to deterioration during operations [2, 3]. In addition, a wireless solution guarantees higher comfort, enhancing user convenience. This technology has gained substantial popularity across various fields, including:

- Transportation: WPT-based charging solutions for electric vehicles come in stationary and dynamic forms. Dynamic solutions, where charging occurs while the vehicle is in motion, have the potential to extend the distance range of electric vehicles and reduce the size and weight of the battery pack. This approach is particularly well-suited for vehicles with predetermined routes, such as buses and trucks [4, 5]. Along with automotive charging systems, those for unmanned aerial vehicles (UAVs) are also being developed [6].
- Healthcare: The application of wireless battery chargers for implantable electronic devices eliminates the need for wired connections between the power source and the devices. This feature enhances patient safety and reduces the energy storage requirements of implantable devices, improving patient comfort [7].
- Consumer electronics: With the proliferation of electronic devices like smartphones, tablets, wearable gadgets, and laptops, the demand for WPT solutions for their charging has grown significantly. This trend has driven the development of WPT technology for these consumer electronics [8, 9].

The range of applications for WPT is not restricted solely to the examples provided. In accordance with the fundamental principles governing power transfer, inductive and capacitive systems can be identified [10]. For the sake of clarity, other methods for WPT systems are also diffused, such as radio frequency waves, optical links, and ultrasound. It is worth noting that, up to now, these methods are primarily utilized for signal transmission or for transferring very low levels of power. This paper focuses on inductive WPT systems, where the power is transferred through the time-varying magnetic field between coupled coils, a transmitter, and a receiver. In an inductive system, there is a non-negligible air gap between the transmitter and receiver coils, and the length of this gap varies depending

on the specific application. The presence of this air gap leads to a significant leakage flux, resulting in a reduced coupling coefficient between the coils [11]. Additional reactive components can be added to form resonant compensation networks and enhance the system's efficiency.

The most commonly used compensation topology for inductive wireless power transfer (IWPT) systems is the series–series (SS) compensation, including a series capacitor on each coil side [12]. Nonetheless, various alternative topologies have been proposed in the literature to provide greater flexibility in system design and regulation. Notably, the LCC-S topology minimizes voltage and current stresses on the passive components compared to SS compensation [13, 14].

Thanks to these characteristics, the LCC-S compensation is widely used for many applications such as charging electric vehicles [15], electric motors [16] and autonomous underwater vehicles [17]. In all these applications, it is essential to regulate the power delivered to the load. For example, in [18], the transferred power is adjusted to recharge a battery with a CC/CV profile by varying the frequency. However, adjusting the power by varying the frequency is not the best solution from a system design point of view. In fact, operating in a frequency range forces the designer to size filters for the lowest frequency, making the system oversized under certain operating conditions. In addition, variable frequency controllers usually make electromagnetic compatibility more challenging [19, 20].

For this reason, in this paper, the transferred power is adjusted by keeping the operating frequency of the inverter constant and varying the compensation input inductor. The choice of the input inductor value in an LCC-S compensated IWPT system directly impacts the power delivered to the load. Therefore, a controlled variable inductor can be employed to achieve output power regulation. This control method, known in the literature as the magnetic control technique, is widely adopted in other resonant converter topologies such as the LLC or DAB resonant converters [21, 22]. The principles of magnetic control can also be applied to regulate power transmission in the context of IWPT systems effectively [23, 24]. There are several methods for implementing the magnetic control strategy. One approach involves reconfiguring discrete inductors using power switches, but this method is costly and results in a bulky design due to the need for multiple components. In [25], a variable inductance is obtained by adjusting the air gap through an inclined or staggered aperture structure. However, this method is complex in terms of manufacturing, leading to higher costs. Another promising approach is to produce a controlled variable inductor by exploiting the magnetic permeability of the material. This goal is achieved by introducing an additional magnetic polarization flux in addition to the primary inductor magnetic flux, causing a shift in magnetic induction, as discussed in [26].

A controlled variable inductor is obtained by preparing a magnetic core with at least two windings. The first, defined as the AC winding, is connected to the resonant tank of the IWPT system, and the second, the DC winding, allows the control of the core magnetization. Thus the differential inductance of the AC winding can be continuously regulated between an unsaturated and an admissible saturated value. The strength of this approach lies in its ability to achieve a broad range of inductance variation with a single inductor. This inductor's value can be adjusted, reducing the size and weight of passive components when compared to the discrete inductor approach. However, using a controlled variable inductor to regulate the IWPT system's output power presents specific challenges. Effectively controlling the magnetizing current in the auxiliary winding with a proper source is needed, requiring the addition of an extra power converter for current control implementation. A suitable solution to efficiently supply the magnetizing winding is a synchronous buck converter operating at low voltage. Another critical aspect of employing a controlled variable inductor in the IWPT system is the non-linear behaviour introduced by the operation in a saturated state. Accurate inductor modelling is essential to assess the performance of the IWPT system during the design phase and to develop an effective control strategy for output power regulation.

This paper, starting from the performed design and simulation of a complete LCC-S compensated IWPT system with a variable inductor, presented in [23, 24], and from the description of the design of a controlled variable inductor for an IWPT system, described in [27], presents the experimental validation of the proposed regulation strategy through a set of measurements devoted to highlight strengths, weaknesses, and future improvements of the method.

For this reason, the main novel contributions of this paper are:

- To propose an auxiliary circuit for the current regulation of the variable inductor in the LCC-S compensation that allows operating at high performance while using a limited number of additional components.
- Since there are currently no experimental validations of this system in the literature, extensive experimental measurements are performed to evaluate the feasibility and performance of this type of system in steady-state conditions.

The paper is structured as follows: in Section 2, the analysis and design considerations of an LCC-S compensated IWPT system are presented, in addition to the design procedure of the controlled variable inductor and the auxiliary circuit for the regulation of the magnetizing current. Section 3 describes the experimental setup used for the validation of the magnetic control strategy applied to the output power regulation of an IWPT system, while, in Section 4, the results of the measurements are presented and described. Finally, in Section 5, the conclusions are derived.

2 | MAGNETIC CONTROL IN LCC-S IWPT SYSTEM

The electrical circuit of the LCC-S compensated IWPT system is described in Figure 1. The structure is supplied by a half-bridge on the transmitter side, while a diode full-wave rectifier is used for the DC load supply on the receiver side.

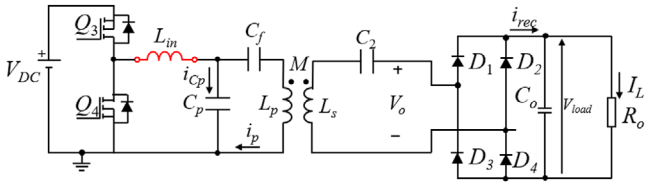

FIGURE 1 Electrical circuit of the LCC-S compensated IWPT system, supplied by a half-bridge converter on the transmitter side. The variable inductor used for the implementation of the magnetic control is represented in red.

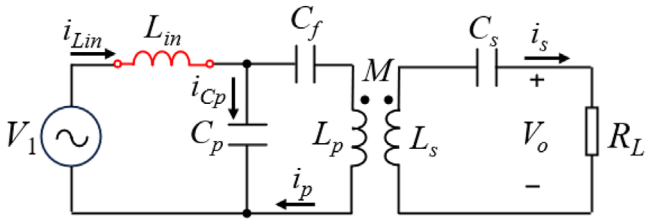

FIGURE 2 Equivalent electrical circuit of the LCC-S compensated IWPT system, considering the first harmonic approximation.

Using the first harmonic approximation (FHA), the circuit in Figure 1 can be approximated with the circuit shown in Figure 2.

The root mean square (RMS) value of the first harmonic of the voltage impressed by the half-bridge inverter is V_1, while the full-wave rectifier is approximated by an equivalent resistor $R_L = (8/\pi^2) \cdot R_o$. To operate in resonant conditions at a particular angular frequency ω_0 and achieve high transmission efficiency, the following design equations are used for the design of the compensation network [13]:

$$\omega_0 L_s = \frac{1}{\omega_0 C_s} \tag{1}$$

$$\omega_0 L_p = \frac{1}{\omega_0 C_p} \tag{2}$$

$$\omega_0 L_{in} = \omega_0 L_p - \frac{1}{\omega_0 C_f} \tag{3}$$

As shown in [28], the expression of the output power and transmission efficiency can be calculated as

$$P_o = \frac{\omega^2 M^2 V_1^2 R_L}{R^2 \omega^2 \left[L_{in} + L_p + \frac{L_{in} C_p}{C_f} \alpha - \frac{1}{\omega^2 C_f} \right]^2 + \gamma^2 \beta^2} \tag{4}$$

$$\eta = \frac{\omega^2 M^2 R_L C_f}{R\beta \left[C_p \left[\omega^2 C_f \left(L_{in} + L_p \right) \right] + \omega^2 L_{in} C_p \alpha - 1 \right] + \gamma \left(C_p + C_f \zeta \right)} \tag{5}$$

where M is the mutual inductance, while the expression of the coefficients α, β, γ, and ζ are shown in [23]. If the system operates in resonant condition, the previous equations can be simplified as

TABLE 1 Parameters of the LCC-S compensated IWPT system.

Parameter	Value	Description
f	85 kHz	Operating frequency
V_{DC}	30 V	DC input voltage
P_o	50 W	Output power
k	0.38	Coupling coefficient
L_p	87.5 μH	Primary coil inductance
L_s	92.96 μH	Secondary coil inductance
R_p, R_s	0.2 Ω	Primary and secondary parasitics
R_L	50 Ω	Load resistance

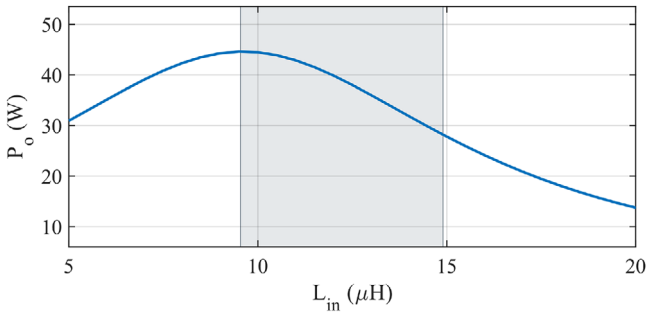

FIGURE 3 Variation of the load power P_o as a function of the input inductance L_{in}.

$$P_o = \frac{\omega^4 C_f^2 M^2 R_L V_1^2}{\left(R_s + R_L\right)^2 \left(\omega^2 C_f L_p - 1\right)^2} \tag{6}$$

$$\eta = \frac{R_L \omega^2 M^2}{\left(R_s + R_L\right)\left(\omega^2 M^2 + \left(R_s + R_L\right) R_p\right)} \tag{7}$$

The best option is to design the system to operate in resonance conditions corresponding to the nominal working conditions in order to guarantee maximum transmission efficiency. Thus, inverting Equation (6), the value of C_f that allows to achievement a particular output power P_o at resonant condition is

$$C_f = \frac{\omega L_p + \sqrt{\omega^2 \left(L_p^2 - M^2 R_L V_1^2\right) - P_o \left(R_s + R_L\right)^2 L_p^2}}{\omega \left[\left(R_s + R_L\right)^2 L_p^2 - \omega^2 M^2 R_L V_1^2 \right]} \tag{8}$$

Once the value of C_f is defined, the values of L_{in}, C_p, and C_s can be easily calculated using Equations (1), (2), and (3). Substituting these values in the Equations (1), (2), (3), and (8), the components values shown in Table 1 can be calculated.

The dependence of the load power as a function of the inductance value of L_{in} is described by Equations (4), and its behaviour for the proposed system is represented by Figure 3, highlighting how the magnetic control strategy can be suitable for the output power regulation of an LCC-S compensated IWPT system. In particular, it can be seen how, given the maximum value of transferred power at approximately 9.5 μH,

there are two options for regulating the output power. The first is to consider the inductance value that gives the maximum power as the unsaturated case, then lead the magnetic component towards saturation to decrease the transferred power. The second is to consider the inductance value that gives the maximum power as the saturated one, thus obtaining the minimum transferred power in the unsaturated configuration. The last option is the one selected since a reduced saturation rate (33% w.r.t 47%) achieves the same output power variation. A further reason to prefer the second regulation option can also be identified since an amount of energy has to be spent to reach the saturated operation of the variable inductor. In order to maximize the overall IWPT system efficiency, it is preferable to spend this extra energy term when the system delivers the maximum output power. Following these considerations, for the analysed IWPT system, we considered an inductance variation range from approximately 15 to 8 μH for the design of the controlled variable inductor described in Section 2.1

2.1 | Structure of the controlled variable inductor

For the proposed IWPT system, we decided to implement the controlled variable inductor by controlling the saturation of a magnetic core by means of an auxiliary winding supplied by a DC current. In particular, a double-E core structure was selected. The double E-core structure allows the placement of the DC magnetizing windings (black) on the outer columns of the core. By connecting them in anti-series, the path of the static magnetic field can be controlled only on the outer legs of the core. The AC winding (red), connected to the transmitter side of the system, is located on the central column of the core. The material of the central leg operates in the linear region of the magnetization since no static magnetic field interests this path, and an air gap ensures low AC magnetic field values, even with considerable voltage and current swings of the AC winding [27]. A further advantage of this configuration is that the anti-series connection of the DC windings almost cancels the sum of the induced electromotive force on each by improving the capability of the magnetization control, which is useful for the transmitted power regulation of the system. Figure 4 describes the presented structure of the controlled variable inductor. For the considered structure, the design of the controlled variable inductor can be performed based on the following considerations: the inductance value L_{in} is a function of the number of turns of the AC winding N_{AC} and the equivalent reluctance $\mathcal{R}_{eq}$ referred to the AC winding:

$$L_{in} = \frac{N_{AC}^2}{\mathcal{R}_{eq}(N_{DC}I_{DC})}, \tag{9}$$

The equivalent reluctance depends on the permeability expressed by the core material, which can be regulated by means of the magnetic field controlled by the current I_{DC} in the auxiliary winding with N_{DC} turns. Thus, the equivalent reluctance

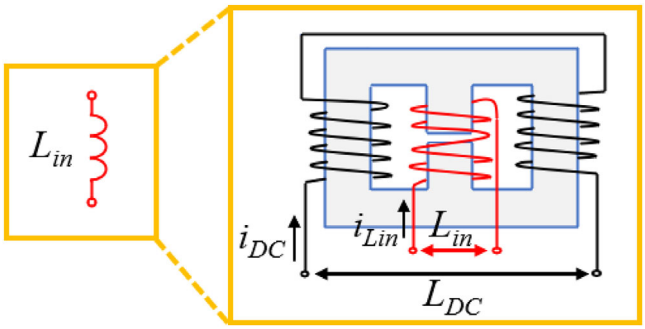

FIGURE 4 Structure of the controlled variable variable inductor, implemented on a double-E ferrite core. The AC winding, connected to the LCC compensation network, is represented in red. The DC windings, connected to the auxiliary circuit for the magnetization control, are represented in black.

can be expressed as

$$\mathcal{R}_{eq}(N_{DC}I_{DC}) = \mathcal{R}_{tot,c} + 0.5\,\mathcal{R}_{tot,l}(N_{DC}I_{DC}). \tag{10}$$

The reluctance of the central column $\mathcal{R}_{tot,c}$ is the of the central magnetic material path reluctance (fe) and the air gap reluctance (g):

$$\mathcal{R}_{tot,c} = \frac{l_{fe,c}}{\mu_0\,\mu_{fe}\,S_{fe,c}} + \frac{l_g}{\mu_0\,S_g}, \tag{11}$$

where $l_{fe,c}$ represents the path length of different core portions, $S_{fe,c}$ is the cross-section, μ_{fe} is the relative permeability of the magnetic material and μ_0 is the vacuum permeability. The reluctance of the central column is assumed to be constant since it is not influenced by the magnetic field caused by the magnetizing current, while the reluctance of the outer column $\mathcal{R}_{tot,l}$ is

$$\mathcal{R}_{tot,l}(N_{DC}I_{DC}) = \frac{l_{fe,l}}{\mu_0\,\mu_{fe}(N_{DC}I_{DC})\,S_{fe,l}}. \tag{12}$$

where the relative permeability of the core material $\mu_{fe}(N_{DC}I_{DC})$ is a function of the DC current in the auxiliary winding, which controls the magnetic field in the outer path of the core. Following this analytical design rules, different cores and winding arrangements can be exploited to find an inductance profile suitable for the output power regulation of the considered LCC-S compensated IWPT system. The core selected for the prototype, described in Figure 5, is a double-E ferrite core (E 32/16/19 N87 ferrite, from TDK). A 1 mm thick air gap is located in the central column of the core.

The realized prototype has the specifications reported in Table 2, while Figure 6 reports the measured differential inductance profile. Further details on the inductor design procedures and design verification by means of finite element simulations are described in detail in [27].

The inductance profile of the variable inductor prototype, reported in Figure 6, is suitable for the inductance variation range of the analysed IWPT system previously described in Section 2.

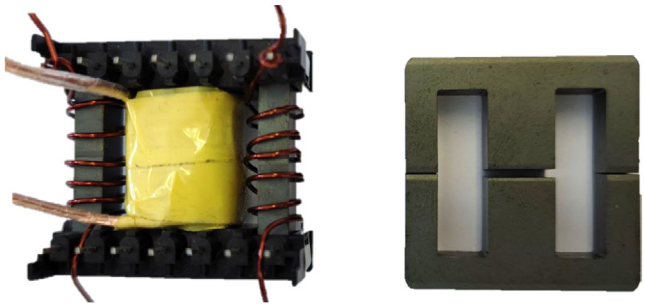

FIGURE 5 Photo of the controlled variable inductor prototype. The adopted N87 ferrite core with a gapped central column is shown on the right.

TABLE 2 Specifications of the realized controlled variable inductor.

Core material	N87 ferrite
Core geometry	E 32/16/9
Air gap length	1 mm
AC winding N turns	10
DC winding N turns	10 (5 + 5)
Nominal inductance @ $I_{DC} = 0$ A	14.9 μH
Saturated inductance @ $I_{DC} = 4$ A	8.3 μH

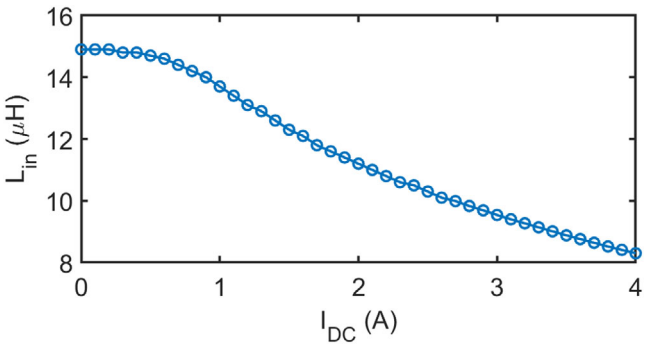

FIGURE 6 Measured differential inductance profile of the realized controlled variable inductor.

2.2 | Inductor power loss estimation

A preliminary power loss estimation for the designed controlled variable inductor can be performed. In this device, three power loss terms exist: the ohmic losses of the AC winding $P_{W,AC}$, the ohmic losses of the DC winding $P_{W,DC}$, and the magnetic core losses P_C. The first term can be estimated by knowing the RMS value of the AC current and the high-frequency resistance of the AC winding. In order to reduce the high-frequency resistance, the AC winding has been prepared with a litz wire. The measured resistance at 85 kHz is $R_{AC} = 24.1$ mΩ [27]. The DC winding losses can be computed on the basis of the auxiliary winding current value and the resistance of the winding, whose measured value is $R_{DC} = 74.3$ mΩ. The estimation of the magnetic core losses is more critical since the different sections of the core operate under different magnetic flux density conditions. In fact, the DC magnetic field bias only involves the outer path of the core when the magnetization winding is supplied. The computation of the magnetic core losses of soft ferrites under DC magnetic field bias is a critical task, but an estimation can be performed through the MagNet AI, a data-driven method to describe core losses under different operating conditions, including different DC bias values [29, 30]. We used the MagNet AI to compute the volumetric core losses for the N87 material under the operating conditions of the considered application. In particular, for the central column losses $P_{C,cen}$, we considered the operating flux density waveform at 85 kHz without DC bias, while for the outer path losses $P_{C,out}$, we also considered the DC bias value corresponding to the operation of the controlled variable inductor in the saturated state. This methodology provides a preliminary estimation, reported in Table 3, of the total power losses P_{TOT} for the controlled variable inductor in the saturated operation (the worst case).

TABLE 3 Estimated power losses of the controlled variable inductor in the saturated operation ($P_o = 50$ W, $I_{DC} = 3$ A).

$P_{W,AC}$ (W)	0.488
$P_{W,DC}$ (W)	0.669
$P_{C,cen}$ (W)	0.088
$P_{C,out}$ (W)	0.659
P_{TOT} (W)	1.904

2.3 | Analysis of the magnetizing current regulation

The regulation of the magnetizing current is a critical aspect of the proposed magnetic control strategy. The supply system of the magnetizing windings should have a high efficiency and a low cost. To preserve the optimal transmission efficiency of the IWPT system, one viable approach is to employ a DC–DC switching converter, which serves to minimize the power losses of the magnetization circuit. In addition, the load of the magnetizing circuit is only represented by the DC windings of the variable inductor, which are an inductive load with low series resistance (at zero frequency). Considering the controlled variable inductor realized for the experimental setup, the DC winding resistance has a value of $R_{DC} = 74.3$ mΩ. The magnetizing current range required to regulate the magnetization of the variable inductor is in the range $I_{DC} = (0 - 3)$ A, thus the steady state output voltage is in the range $V_{mag} = (0 - 223)$ mV. Achieving this significantly low output voltage value necessitates the use of switching devices with minimal voltage drops. The switching circuit can be implemented with MOSFETs characterized by low current and low breakdown voltage, operating in a synchronous buck converter configuration [31]. However, to reduce the current ripple, a high switching frequency of the buck converter would be beneficial. In addition, a higher switching frequency for the supply of the magnetizing current also allows a more precise current regulation. For

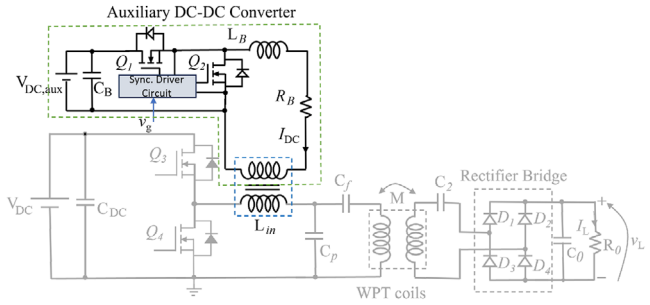

FIGURE 7 Scheme of the experimental setup, with a highlight on the auxiliary DC–DC converter.

this reason, a switching frequency $f_s = 500$ kHz is selected for the experimental setup. At this frequency value, GaN FETs are recommended for this application [32, 33]. In fact, GaN FET devices are characterized by a low conduction resistance ($R_{DS,on} = 2.2$ mΩ) and low breakdown voltage (80 V) and, when operating in a synchronous buck converter configuration, can help to regulate the magnetizing current accurately and reduce the switching losses. The proposed study must be further investigated to determine an effective closed-loop control strategy for output power regulation by means of the magnetizing current regulation.

2.4 | Description of the auxiliary circuit

The auxiliary circuit used for the control of the variable inductor in the proposed system is shown in Figure 7. It consists of a synchronous buck converter with a filtering inductor (L_B), resistor (R_B), and the DC windings of the variable inductor (L_{in}). The inductor L_B is inserted to limit the current ripple of the DC–DC converter while ensuring its operation in the continuous conduction mode. Similarly, R_B is included to limit the maximum DC current supplied by the converter.

The DC–DC converter operates at a switching frequency f_{aux}, and the transistors Q_1 and Q_2 are switched according to the applied duty cycle D.

The output voltage of the buck converter is defined as a function of D as follows:

$$V_{RB} = D \cdot V_{DC,aux} \tag{13}$$

and, hence, the DC current delivered to the DC windings of the inductor L_{in} is:

$$I_{DC} = \frac{D}{R_B} V_{DC,aux} \tag{14}$$

The applied current to the DC winding of the inductor is 0 A for $D = 0$ and has a maximum value of $V_{DC,aux}/R_B$ when $D = 1$. The proposed DC-DC converter can provide high values of I_{DC} with very little $V_{DC,aux}$ if only the equivalent series resistances (ESRs) of L_B and the DC windings of L_{in} are employed. An additional resistor R_B can be included in the DC–DC converter to limit the maximum DC current applied to the inductor, enlarging the range of D that can be applied for achieving an I_{DC} from 0 A to the maximum desired value.

Using an LC meter, the experimental measured ESR of the DC coil was $ESR_{LB} = 122$ mΩ. Since the measured parasitic of the DC winding is $ESR_{DC} = 74.3$ mΩ, for a total series resistance $R_{DC,tot} = 196.3$ mΩ, no external resistance has been used. This solution allowed the power losses of the auxiliary circuit to be kept extremely limited. The auxiliary circuit has been supplied by a low DC voltage source of $V_{DC,aux} = 1.65$ V. With the considered value of the series resistance, a DC current equal to $I_{DC} = 3\,A$ when operating at $D = 0.356$.

TABLE 4 Parameters of the LCC-S compensation network.

Parameter	Analytical	Measured
L_{in}	12.1 μH	14.9 μH
C_p	349.6 nF	353.2 nF
C_f	46.3 nF	43.8 nF
C_s	38.1 nF	33.2 nF

3 | EXPERIMENTAL SETUP

The presented approach for the implementation of the magnetic control applied to an IWPT system is verified by means of an experimental setup. In particular, a half-bridge converter is used for the supply of the transmitter coil. The switching frequency of the half-bridge is 85 kHz, and the duty cycle is fixed at 0.5. The LCC resonant compensation network of the transmitter side is composed of the variable inductor L_{in}, and the two capacitors C_p and C_f, whose values are reported in Table 4.

The variable inductor is produced following the specifications described in 2.1. The supply of the DC winding of the variable inductor is provided with a synchronous buck converter, realized with the development board EPC90122, that contains two EPC2206 enhancement mode (eGaN) field effect transistor (FET). The filtering inductance of the DC–DC converter was set to $L_B = 1$ mH.

The switching frequency of the buck converter has been tested up to 500 kHz. The control signal for the buck converter is provided by an STM32 Nucleo board. The setup has been tested in an open-loop configuration, while in future developments of this research activity, a closed-loop control of the output power through the magnetization current regulation will be provided. Regarding the receiver side, the series compensation capacitor C_s value reported in Table 4 is selected, and a diode full bridge rectifier provides the DC supply for a resistive load of 50 Ω. A picture of the adopted experimental setup is reported in Figure 8.

The input voltage of the system is fixed at 30 V, while the output voltage can be regulated in the range 35-50 V, meaning that the maximum load power selected for the tests is approximately 50 W. In particular, this power transfer condition is achieved with the variable inductor operating in the saturated configuration, while, in the unsaturated case, the transferred power to the

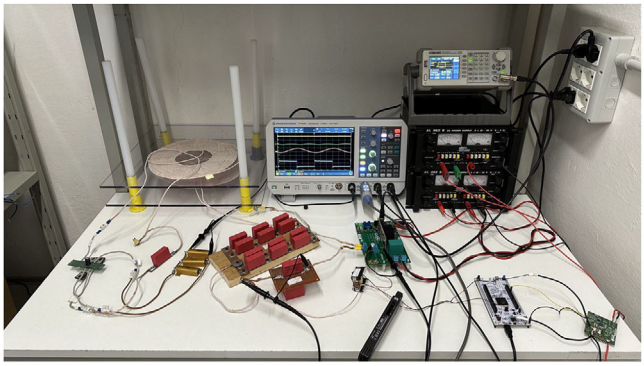

FIGURE 8 Photo of the experimental setup used for validating the principle of the magnetic control applied to the output power regulation of an LCC-S compensated IWPT system.

TABLE 5 Operating conditions of the test cases.

Test number	I_{DC} (A)	V_{load} (V)	P_o (W)	$\eta_{DC\text{-}DC}$ (%)
1	0	35.4	25.1	87.2 %
2	1	38.8	30.1	89.5 %
3	2	44.9	40.5	90.1 %
4	3	51.0	52.1	91.0 %

load is equal to 25 W. This test configuration does not exploit the power capability of the used IWPT system. Still, it is sufficient to effectively validate and test the use of the magnetic control for this kind of application. In order to verify the effectiveness of the proposed output power regulation methodology, several measurements are performed under different operating conditions. The measurements are performed with a digital oscilloscope Rohde & Schwarz RTM3004 (5 GSa/s, 10 bit ADC). The voltage probes are the RT-ZP05S with a 500 MHZ bandwidth, while the current probe is the RT-ZC15B with a 50 MHz bandwidth.

4 | EXPERIMENTAL TESTS RESULTS

To validate the theoretical results, extensive experimental validation has been performed using the setup shown in Figure 8. The performance of the circuit has been evaluated in four different operating conditions varying the DC current I_{DC} of the auxiliary winding of the variable inductor L_{in}. The four tested DC current values and the obtained output power and DC–DC conversion efficiency are shown in Table 5.

In Figure 9, the measured output voltage and conversion efficiency obtained by varying the control inductance L_{in} are shown. In addition, the figure represents the comparison of the experimental voltage measurements with the PLECS circuit simulation results.

The obtained experimental results are in good agreement with the circuit simulation values, confirming the validity of the proposed control system. An in-depth analysis of the power losses is instead shown in Figure 10, where the contribution

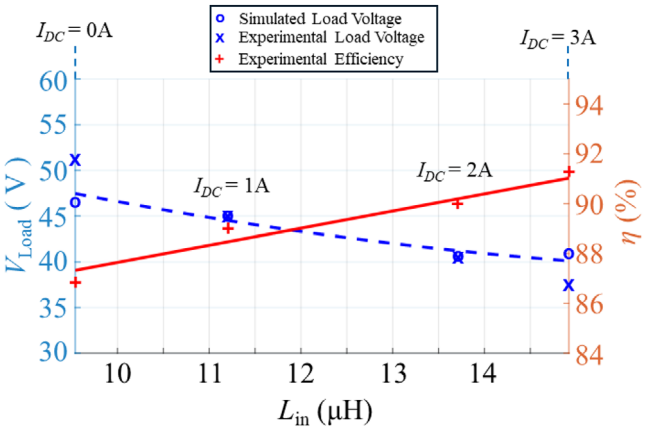

FIGURE 9 Comparison between experimental and PLECS simulation load voltages and conversion efficiency measurements as a function of the input inductance value. The solid and dashed lines represent the interpolation of the experimental results.

of each conversion element is estimated as the four operating conditions vary. In particular, the measured power loss for the capacitors C_f, C_2, and C_p and the transmitter and receiver coils L_1 and L_2 are reported, together with the losses of the transmitter side inverter P_{INV} and the receiver side rectifier P_{RECT}. In addition, the measured power losses of the auxiliary circuit P_{AUX} are reported, taking into account the contribution of the synchronous buck converter and the variable inductor.

As can be seen from the results, the losses introduced by the auxiliary circuit to regulate the current in the variable inductor do not significantly affect the efficiency of the entire system. As expected, this contribution increases as the I_{DC} current increases. However, since an increase in current corresponds to an increase in transferred power, the relative increase in losses remains limited, leading to an overall increase in efficiency, as shown in Table 5 and Figure 9.

Regarding the current and voltage waveforms of the variable inductor, they are shown in Figures 11 and 12. In particular, in Figure 11, the waveforms at zero DC magnetization current for the variable inductor are reported.

The magenta trace represents the inductive current i_L on the transmitter side, the light blue trace represents the voltage over the parallel capacitor C_p, while the green one is the voltage of the half-bridge switching node. The blue signal is the load voltage, which is equal, in this configuration, to 35.4 V, meaning that the power transferred to the load is equal to 25.06 W. The maximum load power condition, whose measurements are reported in Figure 12, is achieved with a magnetizing current $I_{DC} = 3$ A.

In this case, the voltage level on the load is equal to 51 V, corresponding to a transferred power of 52.02 W. For completeness, Table 5 reports all the operating conditions and the measured output power and DC–DC efficiency, while Figure 9 reports the output voltage profile as a function of the input inductance value, by comparing the experimental results with the ones obtained with the analytical model of the LCC-S compensated IWPT system and with the circuit simulations in PLECS.

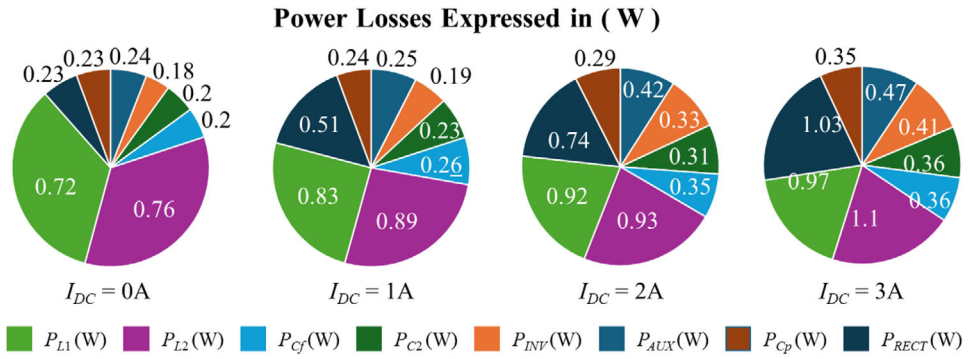

FIGURE 10 Power loss analysis at different operating conditions.

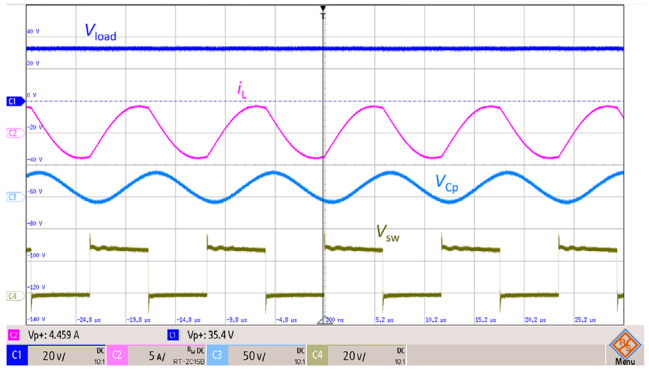

FIGURE 11 Measurements of the load voltage (blue), inductive current on the transmitter side (magenta), voltage on the parallel capacitor C_P (light blue), and voltage of the half-bridge switching node (green), when the DC magnetizing current is set to 0 A and the transferred power is approximately equal to 25 W.

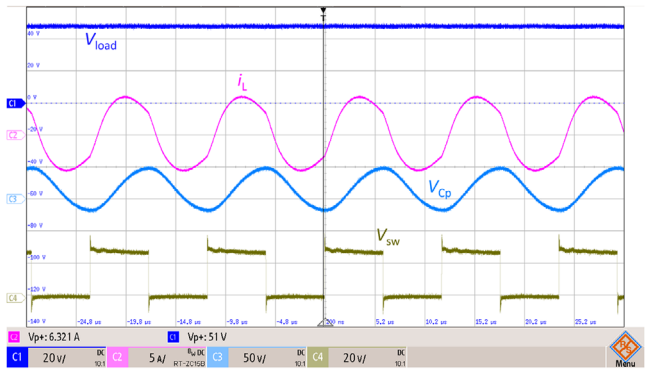

FIGURE 12 Measurements of the load voltage (blue), inductive current on the transmitter side (magenta), voltage on the parallel capacitor C_P (light blue), and voltage of the half-bridge switching node (green), when the DC magnetizing current is set to 3 A and the transferred power is approximately equal to 50 W.

FIGURE 13 Measurements of the load voltage (blue), DC magnetizing current (magenta), and voltage drop over the AC winding of the auxiliary inductor (red), when the DC magnetizing current is set to 1 A and the transferred power is approximately equal to 30 W.

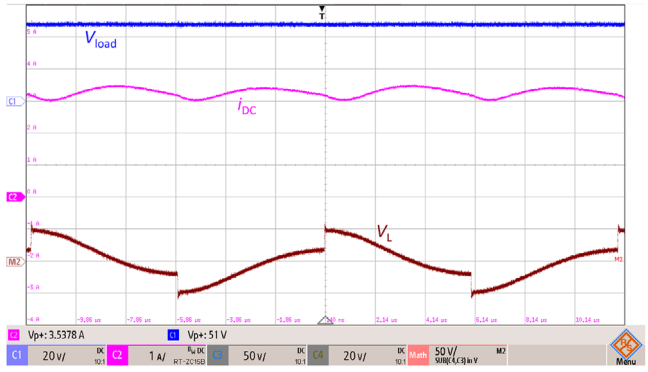

FIGURE 14 Measurements of the load voltage (blue), DC magnetizing current (magenta), and voltage drop over the AC winding of the auxiliary inductor (red), when the DC magnetizing current is set to 3 A and the transferred power is approximately equal to 50 W.

While these preliminary results validate the effectiveness of the magnetic control strategy for the output power regulation of an LCC-S compensated IWPT system, further consideration can be made by looking at the behaviour of the DC magnetizing current of the variable inductor. Figures 13 and 14 represent the measurements of the DC magnetizing current (magenta trace) when regulated at 1 and 3 A, respectively. In addition to the magnetizing current, the acquisition reports the voltage drop over the AC winding of the auxiliary inductor (red trace), and the load voltage (blue trace), to highlight the different operations in terms of transferred output power.

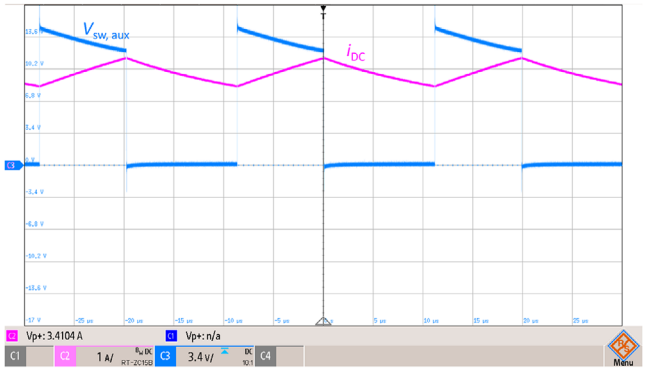

FIGURE 15 Measurements of the DC magnetizing current (magenta), and voltage at the switching node of the buck converter (light blue), when the DC magnetizing current is set to 3 A and the switching frequency of the synchronous buck converter is equal to 50 kHz.

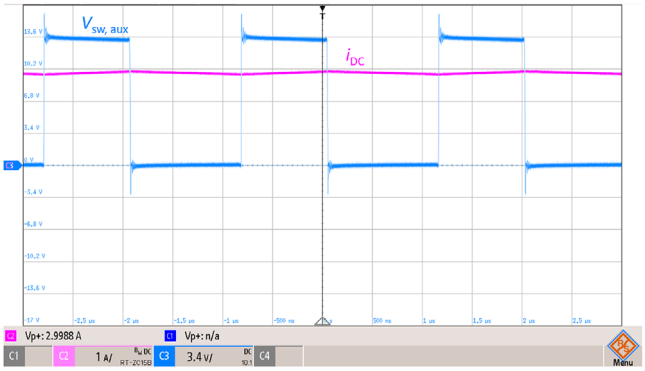

FIGURE 16 Measurements of the DC magnetizing current (magenta), and voltage at the switching node of the buck converter (light blue), when the DC magnetizing current is set to 3 A and the switching frequency of the synchronous buck converter is equal to 500 kHz.

The AC current component, at a fundamental frequency of 85 kHz, is caused by the electromotive force induced in the auxiliary winding related to the magnetic flux produced by the AC winding. In principle, the anti-series connection of the two DC windings makes the sum of the two induced electromotive forces equal to zero. This aspect is fully illustrated in [27]. The measurements show how, for small values of the DC magnetization current, while the variable inductor still operates in a weakly saturated condition, the EMF compensation is effective, and the related current ripple is negligible, as apparent in Figure 13 for $I_{DC} = 1$ A. On the other hand, in the saturated condition, corresponding to $I_{DC} = 3$ A, and represented in Figure 14, the induced EMF-related current ripple is more evident due to the magnetic unbalance of the outer legs of the E core when operating in saturation which causes a non-zero EMF on the series of the two auxiliary windings, and due to the small impedance of the magnetization circuit. In fact, the load of the magnetization circuit is only represented by the inductance and the resistance of the DC windings series. This aspect, already discussed and clarified in [24, 27], does not represent an issue for the load power regulation, and the current ripple can be further reduced by adding a suitable non-saturating inductance on the magnetization circuit and by introducing a current control for the regulation of the buck converter. An additional consideration highlighted by the experimental measurements regards the reduction of the current ripple on the magnetizing circuit obtained by increasing the switching frequency of the buck converter dedicated to the magnetization current regulation. Figures 15 and 16 show the current in the magnetization circuit (magenta trace), when the synchronous buck converter is controlled with a switching frequency of 50 and 500 kHz, respectively, and the target of the magnetizing current is set to 3 A. In addition to the magnetization current, the acquisitions also report the voltage at the switching node of the buck converter (light blue trace).

It is apparent how, the adoption of a higher switching frequency allows a considerable decrease in the current ripple on the magnetizing winding of the variable inductor, improving the accuracy of the magnetization control. The adoption of a GaN-based synchronous buck converter enables the selection of switching frequencies in the range of the hundred of kHz, going in the direction of the reduction of the magnetization current ripple. Figure 17 shows a detail of the current ripple on the magnetizing current when its target value is set to 3 A and the switching frequency of the synchronous buck converter is 85 kHz, highlighting the extremely reduced value if compared to the DC component, which can be assessed at 3.04% (peak to peak).

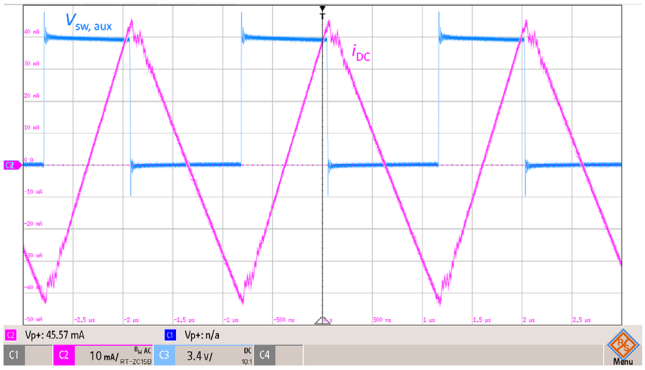

FIGURE 17 Detail of the current ripple of the DC magnetizing current (magenta), and voltage at the switching node of the buck converter (light blue), when the DC magnetizing current is set to 3 A and the switching frequency of the synchronous buck converter is equal to 500 kHz.

5 | CONCLUSIONS

In this paper, the magnetic control for the output power of an LCC-S compensated IWPT system is implemented and experimentally verified. The inductance value of the controlled variable inductor, suitably designed for the proposed experimental setup, is controlled through an auxiliary circuit to regulate the DC magnetization current, implemented with a highly efficient GaN-FET based synchronous buck converter. The effectiveness of the output power regulation through the input inductance control in the LCC-S compensation network

is evaluated and discussed thanks to a set of experimental measurements devoted to testing the real application of the regulation principle. Further improvements for the proposed research are currently running for implementing a closed-loop regulation strategy to control the output power as a function of the applied magnetizing current value.

AUTHOR CONTRIBUTIONS

Luigi Solimene: Conceptualization; formal analysis; investigation; methodology; software; validation; writing—original draft; writing—review and editing. **Fabio Corti**: Conceptualization; formal analysis; investigation; methodology; software; validation; writing—original draft; writing—review and editing. **Salvatore Musumeci**: Conceptualization; formal analysis; funding acquisition; investigation; methodology; supervision; writing—original draft; writing—review and editing. **Francisco López-Alcolea**: Software; validation; writing—original draft; writing—review and editing. **Alberto Reatti**: Formal analysis; funding acquisition; supervision; writing—original draft; writing—review and editing. **Carlo Stefano Ragusa**: Formal analysis; funding acquisition; supervision; writing—original draft; writing—review and editing.

CONFLICT OF INTEREST STATEMENT

The authors declare no conflicts of interest.

DATA AVAILABILITY STATEMENT

Research data are not shared.

ORCID

Luigi Solimene https://orcid.org/0000-0001-5464-1231
Fabio Corti https://orcid.org/0000-0001-8888-0388

REFERENCES

1. Kim, D., Abu-Siada, A., Sutinjo, A.: State-of-the-art literature review of WPT: current limitations and solutions on IPT. Electr. Power Syst. Res. 154, 493–502 (2018). https://doi.org/10.1016/j.epsr.2017.09.018
2. Joseph, P.K., Devaraj, E., Gopal, A.: Overview of wireless charging and vehicle-to-grid integration of electric vehicles using renewable energy for sustainable transportation. IET Power Electron. 12(4), 627–638 (2019). https://doi.org/10.1049/iet-pel.2018.5127
3. Feng, H., Tavakoli, R., Onar, O.C., Pantic, Z.: Advances in high-power wireless charging systems: overview and design considerations. IEEE Trans. Transp. Electrif. 6(3), 886–919 (2020). https://doi.org/10.1109/TTE.2020.3012543
4. Mohammed, S.A.Q., Jung, J.W.: A comprehensive state-of-the-art review of wired/wireless charging technologies for battery electric vehicles: classification/common topologies/future research issues. IEEE Access 9, 19572–19585 (2021). https://doi.org/10.1109/ACCESS.2021.3055027
5. Cirimele, V., Diana, M., Freschi, F., Mitolo, M.: Inductive power transfer for automotive applications: state-of-the-art and future trends. IEEE Trans. Ind. Appl. 54(5), 4069–4079 (2018). https://doi.org/10.1109/TIA.2018.2836098
6. Faraci, G., Raciti, A., Rizzo, S.A., Schembra, G.: Green wireless power transfer system for a drone fleet managed by reinforcement learning in smart industry. Appl. Energy 259, 114204 (2020). https://doi.org/10.1016/j.apenergy.2019.114204
7. Agarwal, K., Jegadeesan, R., Guo, Y.X., Thakor, N.V.: Wireless power transfer strategies for implantable bioelectronics. IEEE Rev. Biomed. Eng. 10, 136–161 (2017). https://doi.org/10.1109/RBME.2017.2683520
8. Xu, W., Liang, W., Peng, J., Liu, Y., Wang, Y.: Maximizing charging satisfaction of smartphone users via wireless energy transfer. IEEE Trans. Mob. Comput. 16(4), 990–1004 (2017). https://doi.org/10.1109/TMC.2016.2577585
9. Lee, E.S., Choi, B.G., Kim, M.Y., Han, S.H.: Optimal number of turns design of the IPT coils for laptop wireless charging. IEEE Access 9, 19548–19561 (2021). https://doi.org/10.1109/ACCESS.2021.3054426
10. Corti, F., Reatti, A., Wu, Y.H., Czarkowski, D., Musumeci, S.: Zero voltage switching condition in class-E inverter for capacitive wireless power transfer applications. Energies 14(4), 911 (2021). https://doi.org/10.3390/en14040911
11. Rituraj, G., Kushwaha, B.K., Kumar, P.: A unipolar coil arrangement method for improving the coupling coefficient without ferrite material in wireless power transfer systems. IEEE Trans. Transp. Electrif. 6(2), 497–509 (2020). https://doi.org/10.1109/TTE.2020.2994091
12. Cho, S.Y., Lee, I.O., Moon, S., Moon, G.W., Kim, B.C., Kim, K.Y.: Series-series compensated wireless power transfer at two different resonant frequencies. In: 2013 IEEE ECCE Asia Downunder, pp. 1052–1058. IEEE, Piscataway, NJ (2013)
13. Yang, J., Zhang, X., Zhang, K., Cui, X., Jiao, C., Yang, X.: Design of LCC-S compensation topology and optimization of misalignment tolerance for inductive power transfer. IEEE Access 8, 191309–191318 (2020). https://doi.org/10.1109/ACCESS.2020.3032563
14. Wang, W., Deng, J., Chen, D., Wang, Z., Wang, S.: A novel design method of LCC-S compensated inductive power transfer system combining constant current and constant voltage mode via frequency switching. IEEE Access 9, 117244–117256 (2021). https://doi.org/10.1109/ACCESS.2021.3105103
15. Chen, Y., Zhang, H., Park, S.J., Kim, D.H.: A switching hybrid LCC-S compensation topology for constant current/voltage EV wireless charging. IEEE Access 7, 133924–133935 (2019). https://doi.org/10.1109/ACCESS.2019.2941652
16. Ding, W., Li, K., Yuan, J., Li, J., Du, C.: Wireless power transmission-based in-wheel switched reluctance motor drive system with an x-type converter. IEEE Trans. Energy Convers. 38(1), 450–462 (2023). https://doi.org/10.1109/TEC.2022.3204179
17. Mostafa, A., Wang, Y., Tangirala, S., Zhang, H., Lu, F.: A 5 kW hull-compatible inductive charging system with 360o folded spatial unipolar coupler for autonomous underwater vehicles (AUVs). IEEE Trans. Ind. Appl. 59(6), 7001–7012 (2023). https://doi.org/10.1109/TIA.2023.3307117
18. Deng, J., Mao, Q., Wang, W., Li, L., Wang, Z., Wang, S., et al.: Frequency and parameter combined tuning method of LCC–LCC compensated resonant converter with wide coupling variation for EV wireless charger. IEEE J. Emerg. Sel. Top. Power Electron. 10(1), 956–968 (2022). https://doi.org/10.1109/JESTPE.2021.3077459
19. Hosseinipour, M., Soorki, M.N., Ahmadian, M.: On effective electromagnetic shielding of modern pulse width modulating adjustable speed drives. IEEE Trans. Electromagn. Compat. 60(4), 875–884 (2018). https://doi.org/10.1109/TEMC.2017.2738840
20. Zhao, X., Jiang, D., Chen, J., Wang, Z., Liu, Z.: The impact of periodic variable switching frequency modulation on power transmission in dual-active-bridge converter and an improved scheme. IEEE Trans. Power Electron. 38(11), 13966–13976 (2023). https://doi.org/10.1109/TPEL.2023.3302428
21. Wei, Y., Luo, Q., Mantooth, A.: Comprehensive analysis and design of LLC resonant converter with magnetic control. CPSS Trans. Power Electron. Appl. 4(4), 265–275 (2019). https://doi.org/10.24295/CPSSTPEA.2019.00025
22. Wei, Y., Luo, Q., Du, X., Altin, N., Alonso, J.M., Mantooth, H.A.: Analysis and design of the LLC resonant converter with variable inductor control based on time-domain analysis. IEEE Trans. Ind. Electron. 67(7), 5432–5443 (2020). https://doi.org/10.1109/TIE.2019.2934085
23. Solimene, L., Corti, F., Musumeci, S., Reatti, A., Ragusa, C.S.: A controlled variable inductor for an LCC-S compensated wireless power transfer system. In: IECON 2022–48th Annual Conference of the IEEE Industrial Electronics Society, pp. 1–6. IEEE, Piscataway, NJ (2022)

24. Solimene, L., Corti, F., Musumeci, S., Ragusa, C.S., Reatti, A.: Magnetic control of LCC-S compensated wireless power transfer system. In: 2022 International Symposium on Power Electronics, Electrical Drives, Automation and Motion (SPEEDAM), pp. 160–165. IEEE, Piscataway, NJ (2022)
25. Wolfle, W.H., Hurley, W.G.: Quasi-active power factor correction with a variable inductive filter: theory, design and practice. IEEE Trans. Power Electron. 18(1), 248–255 (2003). https://doi.org/10.1109/TPEL.2002.807135
26. Alonso, J.M., Perdigão, M., Dalla Costa, M.A., Zhang, S., Wang, Y.: Variable inductor modeling revisited: the analytical approach. In: 2017 IEEE Energy Conversion Congress and Exposition (ECCE), pp. 895–902. IEEE, Piscataway, NJ (2017)
27. Solimene, L., Corti, F., Musumeci, S., Ragusa, C.S., Reatti, A., Cardelli, E.: Design and modelling of a controlled saturable inductor for an LCC-S compensated WPT system. J. Magn. Magn. Mater. 564, 170056 (2022). https://doi.org/10.1016/j.jmmm.2022.170056
28. Qi, J.: Analysis, design, and optimisation of an LCC/S compensated WPT system featured with wide operation range. IET Power Electron. 13(9), 1819–1827 (2020). https://doi.org/10.1049/iet-pel.2019.1305
29. Li, H., Serrano, D., Wang, S., Chen, M.: MagNet-AI: neural network as datasheet for magnetics modeling and material recommendation. IEEE Trans. Power Electron. 38(12), 15854–15869 (2023). https://doi.org/10.1109/TPEL.2023.3309233
30. MagNet AI. https://mag-net.princeton.edu/. Accessed 9 Feb 2024
31. Armando, E., Fusillo, F., Musumeci, S., Scrimizzi, F.: Low voltage trench-gate MOSFETs for high efficiency auxiliary power supply applications. In: 2019 International Conference on Clean Electrical Power (ICCEP), pp. 165–170. IEEE, Piscataway, NJ (2019)
32. Sun, R., Lai, J., Chen, W., Zhang, B.: GaN power integration for high frequency and high efficiency power applications: a review. IEEE Access 8, 15529–15542 (2020). https://doi.org/10.1109/ACCESS.2020.2967027
33. Barba, V., Solimene, L., Palma, M., Musumeci, S., Ragusa, C.S., Bojoi, R.: Modelling and experimental validation of GaN based power converter for LED driver. In: 2022 IEEE International Conference on Environment and Electrical Engineering and 2022 IEEE Industrial and Commercial Power Systems Europe (EEEIC / I&CPS Europe), pp. 1–6. IEEE, Piscataway, NJ (2022)

How to cite this article: Solimene, L., Corti, F., Musumeci, S., López-Alcolea, F.J., Reatti, A., Ragusa, C.S.: Experimental validation of magnetic control strategy in LCC-S compensated wireless power transfer systems. IET Power Electron. 17, 919–929 (2024). https://doi.org/10.1049/pel2.12718